SCIENCE CHINA
Information Sciences

• RESEARCH PAPER •

April 2022, Vol. 65 142402:1–142402:13
https://doi.org/10.1007/s11432-020-3057-y

Mode-localized accelerometer with ultrahigh sensitivity

Hao KANG, Bing RUAN, Yongcun HAO & Honglong CHANG*

Ministry of Education Key Laboratory of Micro and Nano Systems for Aerospace, School of Mechanical Engineering,
Northwestern Polytechnical University, Xi'an 710072, China

Received 2 April 2020/Revised 3 June 2020/Accepted 7 August 2020/Published online 6 September 2021

Abstract The mode localization phenomenon is an effective technique to enhance sensor sensitivity, and some low noise floor mode-localized sensors, including accelerometers, mass sensors, and electrometers, have been successfully realized. To further improve the performance of the mode-localized accelerometer, we report a microelectromechanical system mode-localized accelerometer based on 4-degree of freedom (DoF) weakly coupled resonators (WCRs) with a stress-relief structure eliminating the thermal stress generated during the silicon-on-glass fabrication process. Experimental results show that compared with the state-of-the-art 3-DoF mode-localized accelerometer (4.40 g^{-1}), the amplitude ratio-based sensitivity of the proposed accelerometer (119.36 $\text{V}\cdot\text{g}^{-1}$) is improved by 2612%. Moreover, the noise floor is 0.64 $\mu\text{g}\cdot\text{Hz}^{-1/2}$ from 0.01 to 3 Hz under the closed-loop circumstance. To the authors' best knowledge, this is the lowest measured noise floor for mode-localized accelerometers.

Keywords mode localization, weakly coupled resonators, accelerometer, degree-of-freedom, microelectromechanical system

Citation Kang H, Ruan B, Hao Y C, et al. Mode-localized accelerometer with ultrahigh sensitivity. Sci China Inf Sci, 2022, 65(4): 142402, https://doi.org/10.1007/s11432-020-3057-y

1 Introduction

Over the past few decades, microelectromechanical system (MEMS) accelerometers have become an important type of accelerometer owing to their various applications in automotive and consumer electronics. The noise floor of MEMS accelerometers is constantly improving and is being used to detect feeble fluctuant signals such as earth tides [1] and earthquakes [2].

The state-of-the-art accelerometers with ultrahigh sensitivity are mostly based on the ultralarge proof mass [3–5]. In this study, we propose an ultrahigh sensitivity accelerometer based on the mode localization phenomenon, which has been recently used for developing various high-sensitivity resonant sensors, such as mass sensors [6, 7], force sensors [8, 9], accelerometers [10–14], and electrometers [15, 16]. In structure dynamics, mode localization is an extension of Anderson localization in the field of solid-state physics and is usually manifested in the periodic structure of weakly coupled resonators (WCRs). When a small disorder is applied, the mode shape of the WCRs will be drastically changed and the vibration energy will mostly be confined to some specific modes of the WCRs [17]. In this method, the sensitivity is amplified by the energy confinement of the mode localization phenomenon, thus enabling an obvious increase in the sensitivity even if the proof mass is small. The sensing scheme based on mode localization enables the sensor's high sensitivity and low-noise floor and rejects environmental common mode noises such as temperature [18–20] and pressure [21].

The amplification of sensitivity and noise floor of the mode-localized sensor is proportional to the number of the degree of freedoms (DoFs) in the WCRs, as observed in 2-DoF (181 $\mu\text{g}\cdot\text{Hz}^{-1/2}$) and 3-DoF (32.7 $\mu\text{g}\cdot\text{Hz}^{-1/2}$) mode-localized accelerometers [6, 7] characterized using the fast Fourier transform (FFT) method. Therefore, the mode-localized accelerometer with large DoFs is an alternative to achieve

---

* Corresponding author (email: changhl@nwpu.edu.cn)

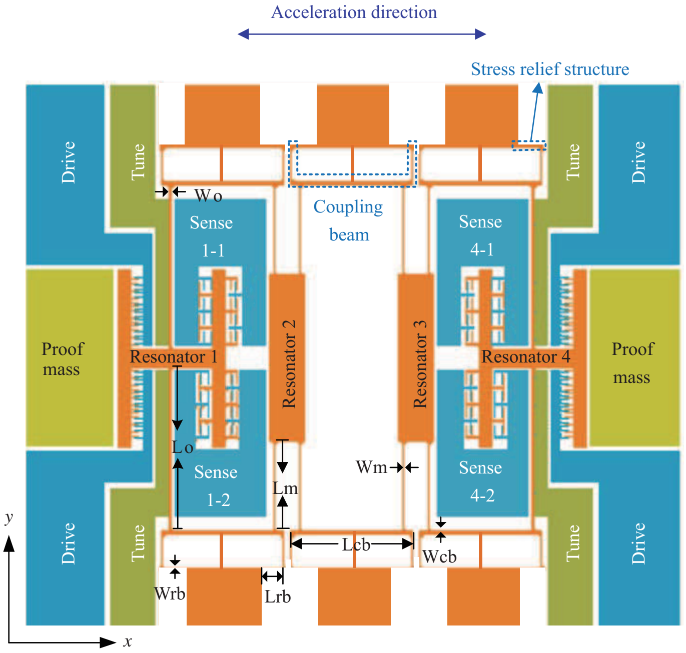

Figure 1 (Color online) Schematic of the 4-DoF mode-localized accelerometer.

a low noise floor accelerometer. However, a large DoF system is difficult to implement owing to severe feedthrough and dense mode distribution, implying that the resonance frequency difference of the first two modes is quite small. In a previous study [22], an electrically coupled 4-DoF mode-localized accelerometer was demonstrated. However, this accelerometer was measured only under open-loop circumstances and showed no expected performance improvement. In this study, we demonstrate a 4-DoF mode-localized accelerometer realized by mechanical coupling instead of electrostatic coupling [19] for better coupling stability. Furthermore, under the closed-loop circumstance, the current mode-localized sensors are single-input and dual-output systems because the amplitude ratio is used as an output metric; thus, there are two output channels. In this study, a divider circuit was proposed to enable an accelerometer with a single input and output. The experimental results showed that a remarkable improvement was achieved in the sensitivity and noise floor of the 4-DoF mode-localized accelerometer.

2 Device design and theory analysis

2.1 Device design

Figure 1 shows a schematic of the 4-DoF accelerometer. Adjacent resonators are weakly coupled using two "E" type coupling beams. Two proof masses located on the outer sides of resonators 1 and 4, respectively, are used to sense acceleration. Tune electrodes are used to change the resonator's effective stiffness to adjust the initial working point. Resonators 1 and 4 are driven by comb fingers and sensed by differential parallel-plate capacitors, which are intentionally designed to eliminate the feedthrough signal from the driving electrodes. Two limit blocks are set at the side of each proof mass in the acceleration direction to avoid a large displacement caused by the strong shock. Moreover, the gap between the proof mass and limit block is 2.5 μm to limit the maximum amplitude of proof mass to 2.5 μm.

Furthermore, for each resonator, two stress-relief structures are designed between the coupling beam and anchor (Figure 1). When thermal stress is generated in the device layer during the fabrication process, the stress-relief structure will deform in the y direction owing to the small stiffness in this direction. Thus, there is no displacement in the x direction (i.e., vibration direction) of the resonator. The stress-relief structures ensure the symmetry of the initial gap of the differential detection capacitor and the effect of the elimination of the feedthrough signal. Table 1 shows the dimension parameters of the designed stress-relief structure.

Table 1 Parameter of the accelerometer

Parameter	Value	Unit
Outer resonator beam length Lo	445	µm
Outer resonator beam width Wo	6	µm
Middle resonator beam length Lm	195	µm
Middle resonator beam width Wm	5	µm
Coupling beam length Lcb	492	µm
Coupling beam width Wcb	10	µm
Stress relief structure length Lrb	150	µm
Stress relief structure width Wrb	8	µm
Device thickness	50	µm
Finger gap	2.5	µm
Outer resonator beam stiffness	74	$\mathrm{N{\cdot}m^{-1}}$
Middle resonator beam stiffness	208	$\mathrm{N{\cdot}m^{-1}}$
Coupling factor	0.028	–
Proof mass value	0.266	mg
Proof mass stiffness	34.7	$\mathrm{N{\cdot}m^{-1}}$

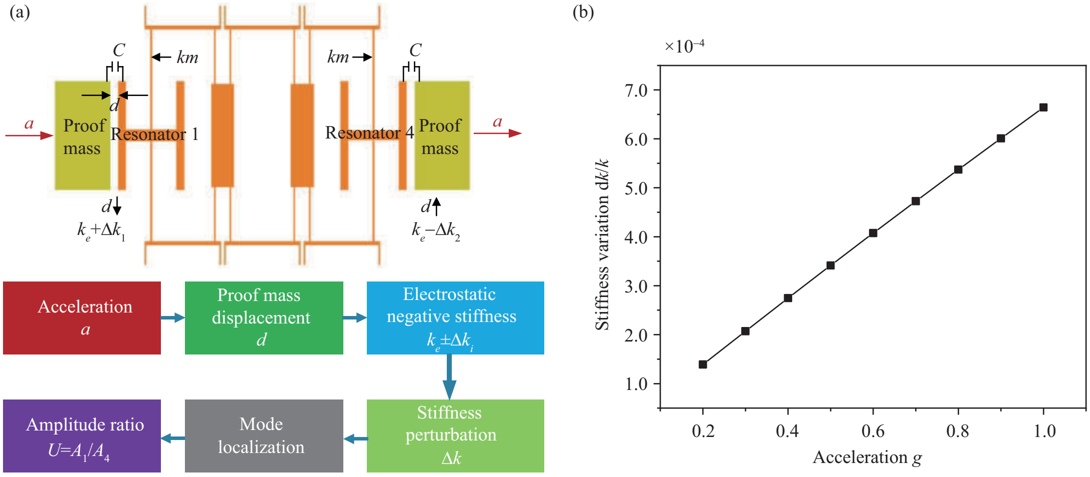

Figure 2 (Color online) (a) Acceleration-sensing mechanism. (b) Variation in the simulated stiffness with the input acceleration.

2.2 Sensing mechanism

Figure 2(a) shows the entire acceleration-sensing mechanism. Electrostatic negative stiffness is introduced in the system by the potential difference between the proof masses and resonators. The gap of the acceleration-sensing capacitors changes when the acceleration acts on the proof mass. Hence, the electrostatic negative stiffness changes. The stiffness perturbation applied to the 4-DoF WCRs system induces the mode localization phenomenon, and the amplitude ratio between resonators 1 and 4 is drastically changed. Finally, the acceleration is obtained by measuring the amplitude ratio between resonators 1 and 4. Table 1 lists the parameters of the accelerometer. The change in the electrostatic negative stiffness caused by acceleration is

$$\Delta k_e(a) = -\frac{\varepsilon A V^2}{d_0^3} + \frac{\varepsilon A V^2}{\left(d_0 + \frac{ma}{k_p+k_e}\right)^3}, \tag{1}$$

where A is the overlap area of the acceleration-sensing capacitors, d_0 is the initial gap of the acceleration-sensing capacitors, V is the potential difference between the proof masses and resonators, m is the mass of the proof mass, a is the acceleration, k_p is the mechanical stiffness of the proof mass, and k_e is the initial electrostatic negative stiffness between the proof mass and resonator. The variation in the stiffness of the resonator is a linear function of an input acceleration, and the variation in the simulated stiffness with the input acceleration is shown in Figure 2(b).

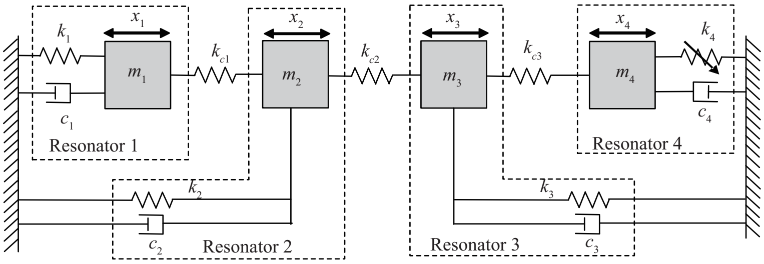

Figure 3 The lumped parameter block diagram of the 4-DoF accelerometer.

2.3 Sensitivity analysis

Figure 3 shows the lumped parameter block diagram of the 4-DoF accelerometer. The damping of each resonator is fairly small because the accelerometer is packaged in high vacuum. To simplify the model, the damping is neglected [23], i.e., $c_1 = c_2 = c_3 = c_4 = 0$. The masses and coupling stiffness of each resonator are assumed to be identical, i.e., $m_1 = m_2 = m_3 = m_4 = m$ and $k_{c1} = k_{c2} = k_{c3} = k_c$. The initial stiffness of resonators 1 and 4 are assumed to be identical, i.e., $k_1 = k_4 = k$, and the stiffness of resonators 2 and 3 are assumed to be identical, i.e., $k_2 = k_3 = k_m$. Because the acceleration-induced stiffness perturbation to the two outer resonators is opposite, assuming that the effective stiffness perturbation Δk is only applied to resonator 4. The dynamic equations of the 4-DoF WCRs are given by

$$\begin{bmatrix} m & 0 & 0 & 0 \\ 0 & m & 0 & 0 \\ 0 & 0 & m & 0 \\ 0 & 0 & 0 & m \end{bmatrix} \begin{bmatrix} \ddot{x}_1 \\ \ddot{x}_2 \\ \ddot{x}_3 \\ \ddot{x}_4 \end{bmatrix} + \begin{bmatrix} k + k_c & -k_c & 0 & 0 \\ -k_c & k_m + 2k_c & -k_c & 0 \\ 0 & -k_c & k_m + 2k_c & -k_c \\ 0 & 0 & -k_c & k + k_c + \Delta k \end{bmatrix} \begin{bmatrix} x_1 \\ x_2 \\ x_3 \\ x_4 \end{bmatrix} = \begin{bmatrix} 0 \\ 0 \\ 0 \\ 0 \end{bmatrix}, \tag{2}$$

where x_i ($i = 1$, 2, 3, and 4) are the displacements of each respective resonator. The frequencies ω_i ($i = 1$, 2) and amplitude ratios U_i ($i = 1$, 2) of the first two modes can be derived as

$$\omega_1^2 = \frac{2\Delta k + k + k_2 - 2k_c - \sqrt{(k - k_m)^2 + 4k_c^2}}{2m}, \tag{3}$$

$$\omega_2^2 = \frac{2\Delta k + k + k_m - \sqrt{(k - k_m)^2 - 4k_c(k - k_m - 2k_c)}}{2m}, \tag{4}$$

$$U_i \approx \left| \frac{-\frac{\Delta k}{k} \cdot \beta \pm \sqrt{(\frac{\Delta k}{k} \cdot \beta)^2 + \kappa^6}}{\kappa^3} \right| \approx \frac{3\varepsilon m A V^2 (5\eta^2 - 9\eta + 4)}{5 d_0^4 k_p k \kappa^3} \cdot a + 1, \tag{5}$$

where β, coupling factor κ and η are defined, respectively, as

$$\beta = \frac{1}{2}\eta^2 - \frac{9}{10}\eta + \frac{2}{5}, \tag{6}$$

$$\kappa = \frac{k_c}{k}, \tag{7}$$

$$\eta = \frac{k_m}{k}. \tag{8}$$

Then, the normalized sensitivity based on the amplitude ratio of the 4-DoF WCRs can be given as

$$S_k^{\text{4-DoF},u} = \left| \frac{\partial(\frac{\Delta u}{u_0})}{\partial(\frac{\Delta k}{k})} \right| \approx \frac{5\eta^2 - 9\eta + 4}{5\kappa^3}. \tag{9}$$

From (9), it can be seen that the sensitivity of the 4-DoF WCRs becomes larger when k_c is smaller and η is larger because both the small stiffness of the coupling beam and larger stiffness of the middle resonator can result in a weaker coupling between the two outer resonators, thus inducing a more severe mode localization effect. With the same coupling factor, the sensitivity of the 4-DoF WCRs is nearly

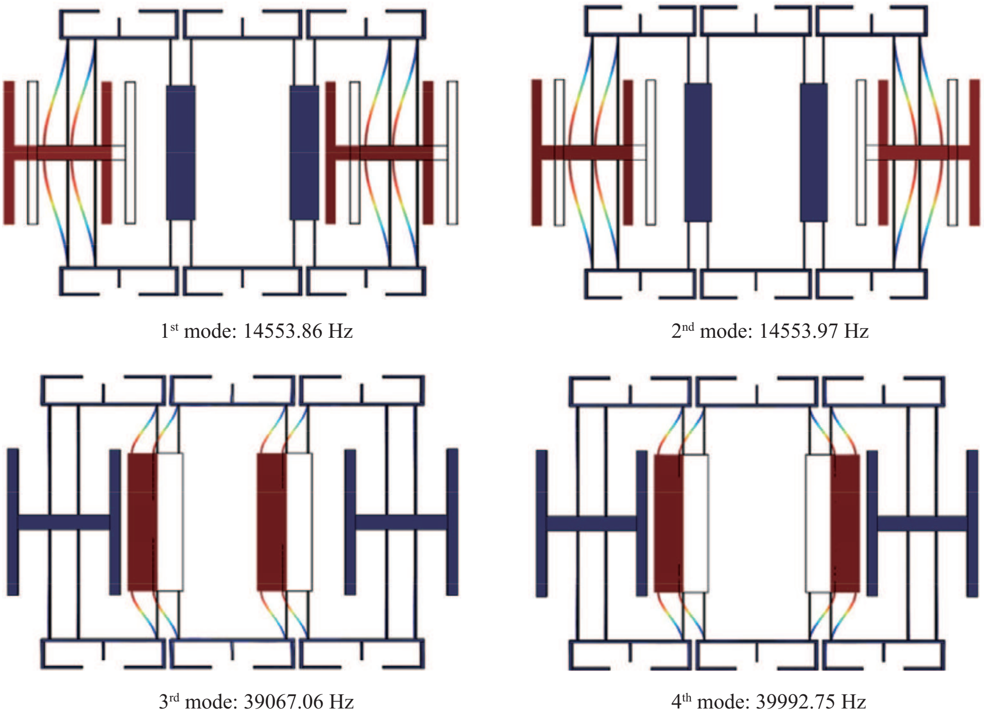
1st mode: 14553.86 Hz

2nd mode: 14553.97 Hz

3rd mode: 39067.06 Hz

4th mode: 39992.75 Hz

Figure 4 (Color online) Vibration modes of the 4-DoF WCRs.

two and four orders larger than 3-DoF and 2-DoF WCRs, respectively. Therefore, the output signal of the 4-DoF WCRs accelerometer can achieve a remarkable enhancement and consequently, considerably lower noise floor.

The design target is to dramatically increase the sensitivity of the WCRs to improve the noise floor of the accelerometer. The designed stiffness of the middle resonators is 6.88 times larger than that of the outer resonators because higher η can increase the sensitivity according to (9). The smaller κ also increases the sensitivity; however, the frequency difference between the first two modes also becomes smaller, as analyzed in Subsection 2.4. Finally, the frequency difference is set as 0.11 Hz and κ is 0.028. Substituting the stiffness of all resonators and coupling factors as shown in Table 1 into (9), the sensitivity of the 4-DoF WCRs with respect to stiffness perturbation ($\Delta k/k$) is calculated to be 149902.

2.4 Vibration modes

Four in-plane vibration modes for the 4-DoF WCRs are simulated in COMSOL software (Figure 4). In the first mode (in-phase mode), two outer resonators vibrate in the same direction, while two middle resonators are nearly stationary because the stiffness of the two middle resonators is set at almost 6.88 times larger than those of two outer resonators. Thus, the sensitivity is further improved and the interference from the third and fourth modes is avoided. In the second mode (out-of-phase mode), two outer resonators vibrate in opposite directions, while two middle resonators are also nearly stationary. In the third mode, two middle resonators vibrate in the same direction, while two outer resonators are nearly stationary. In the fourth mode, two middle resonators vibrate in opposite directions, while two outer resonators are nearly stationary. The in-phase and out-of-phase modes are used as working modes in this study. The simulated resonance frequency of the in-phase and out-of-phase modes are 14553.86 and 14553.97 Hz, respectively, and the resonance frequency difference is 0.11 Hz.

A smaller κ of the WCRs corresponds to a smaller frequency difference Δf of the first two modes; however, the effect differs for the WCRs with different DoFs. Figure 5 shows the relationship between the frequency difference between the first two modes and the κ of the WCRs with different DoFs. Some common WCRs parameters are assumed, i.e., the stiffness of the outer and middle resonators is 100 $\mathrm{N{\cdot}m^{-1}}$ and 200 $\mathrm{N{\cdot}m^{-1}}$, respectively, and the mass of the resonator is 6.27×10^{9} kg. Figure 5 shows the relationship between Δf and κ of WCRs with different DoFs according to the resonance frequency of the first two modes (Eqs. (3) and (4)). When $\kappa = 0.05$, Δf of 2-DoF is 981.03 Hz, while that of the 4-DoF WCRs

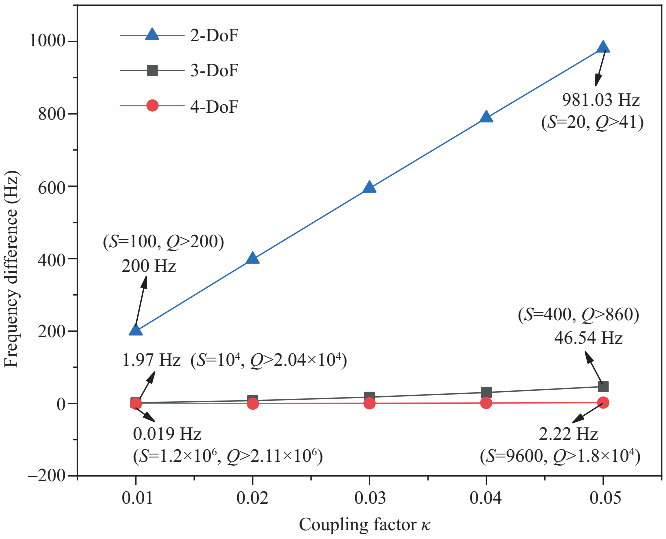

Figure 5 (Color online) Relationship between the frequency difference of the first two modes and the coupling factor of the WCRs with different DoFs.

is only 2.22 Hz. Δf decreases with κ. When $\kappa = 0.01$, Δf of the 2-DoF WCRs is reduced to 200 Hz, while that of the 4-DoF WCRs is only 0.019 Hz. Δf of the WCRs with the same κ will sharply decrease as the DoF number increases because the WCRs with higher DoF have a severe mode localization effect, resulting in a denser mode distribution; thus, the resonant frequencies of the first two modes are closer than those of the WCRs with smaller DoF. Although the sensitivity of the WCRs with higher DoF can be significantly enhanced, Δf will also be very small, which makes it difficult to design and fabricate the device. Moreover, to avoid mode aliasing, which means that the resonance peaks of two modes overlap and cannot be clearly distinguished, Δf should satisfy the following equation:

$$\Delta\omega > 2 \times \Delta\omega_{-3\ \mathrm{dB}} = 2 \times \frac{1}{Q}\omega_0. \tag{10}$$

From (10), it can be seen that quality factor Q of the WCRs must be sufficiently large to obtain a narrow −3-dB bandwidth. According to (10), the minimum Q for the WCRs with different κ can be obtained. From Figure 4, the Q of 4-DoF WCRs with $\kappa = 0.01$ must be larger than 2.11×10^6 and that of 2-DoF WCRs with the same κ only needs to be larger than 200 to avoid mode aliasing. Generally, it is difficult to realize a WCRs with higher DoF.

3 Fabrication and experimental setup

3.1 Device fabrication

The fabrication process of the mode-localized sensors is fully compatible with the current popular MEMS fabrication technology, such as silicon on insulator (SOI) [24] and silicon on glass (SOG). In this study, the accelerometer was fabricated using a standard SOG process with an SOI wafer with a thickness of 464 (400 + 4 + 60) μm. The major fabrication steps are shown in Figure 6(a): (i) photoresist deposition and patterning, (ii) 10-μm groove etching, (iii) bonding with glass, (iv) removal of handle and oxide layers of SOI, (v) photoresist deposition and patterning, (vi) gold deposition, (vii) gold electrode patterning, (viii) photoresist deposition and patterning, and (ix) front-side structure etching and removal of photoresist. Then, the wafer was diced using the grinding wheel. Finally, the devices were packaged in a vacuum environment. Figure 6(b) shows the optical image of the fabricated accelerometer.

During bonding between silicon and glass, the maximum temperature of 633.15 K was achieved. When the temperature was decreased to room temperature, different shrinkage deformation occurred owing to the large difference in thermal expansion coefficients (TEC) of silicon and glass. Because the glass TEC is larger than the Si TEC, the shrinkage of glass is larger to generate thermal stress in the Si layer. This thermal stress causes the resonator anchors on both sides to move inward, which induces compressive

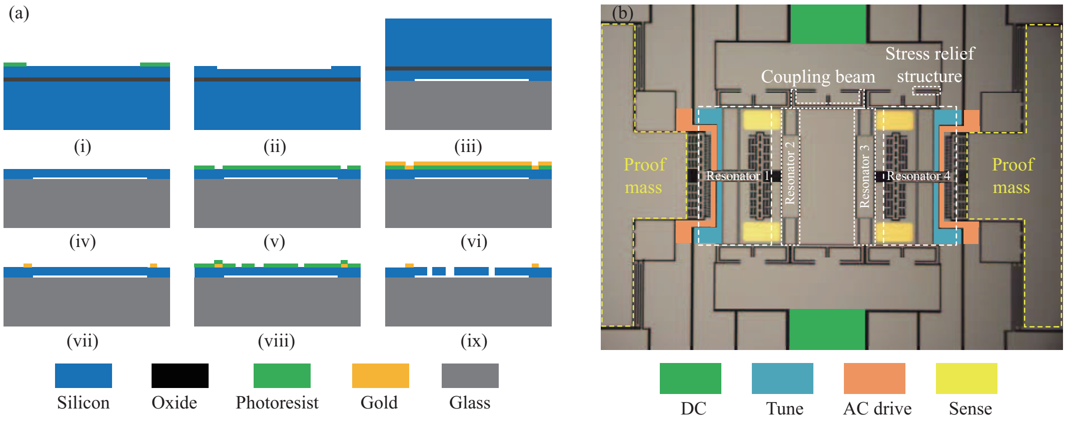

Figure 6 (Color online) (a) SOG fabrication process of the accelerometer. (b) Optical image of the fabricated 4-DoF mode-localized accelerometer.

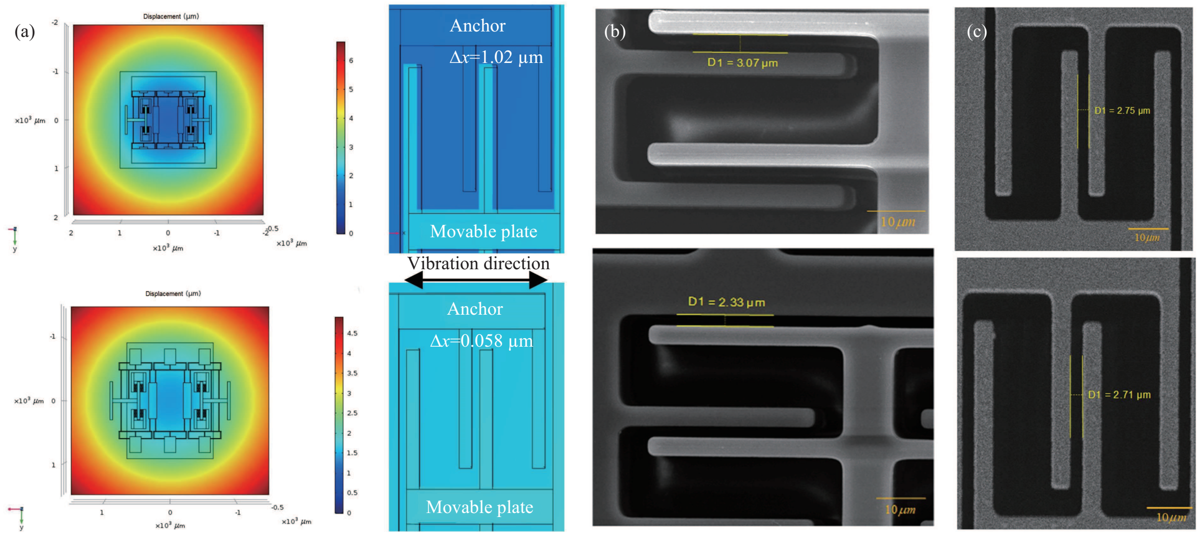

Figure 7 (Color online) (a) Thermal stress simulation of the WCRs without and with the stress-relief structure and displacement of the capacitor plate. (b) The capacitor plate initial gap of the accelerometer without the stress-relief structure. (c) The capacitor plate initial gap of the accelerometer with the stress-relief structure.

stress on the support beam of the resonator. For a conventional resonator without a stress-isolation structure, the resonator was deformed in the vibration direction because of the thermal stress. Then, the initial gap of the sense-plate capacitor is not completely symmetrical, which affects the elimination of the feedthrough signal. However, there is almost no displacement in the x direction for the resonator with the stress-relief structure. Figure 7(a) shows the COMSOL simulations for the above two cases. When thermal stress is applied to the resonator, the relative displacement of the moving and fixed plates of the sensing capacitor without the stress-relief structure is 1020 nm and that of the resonator with the stress-relief structure is 58 nm. Thus, the stress-relief structure significantly reduces the influence of thermal stress on the resonator.

Figures 7(b) and (c) show the fabricated capacitor plate of the accelerometer without and with the stress-relief structure, respectively. The initial gap difference between the pair of differential detection capacitors of the accelerometer without the stress-relief structure is approximately 0.74 μm (2.33 and 3.07 μm) and that of the accelerometer with the stress-relief structure is only approximately 0.04 μm (2.75 and 2.71 μm), which is typically consistent with results of the COMSOL simulation analysis.

3.2 Measurement circuit

The frequency responses of the 4-DoF mode-localized accelerometer with no acceleration input were measured using the open-loop measurement setup, as shown in the open-loop part in Figure 8. A DC

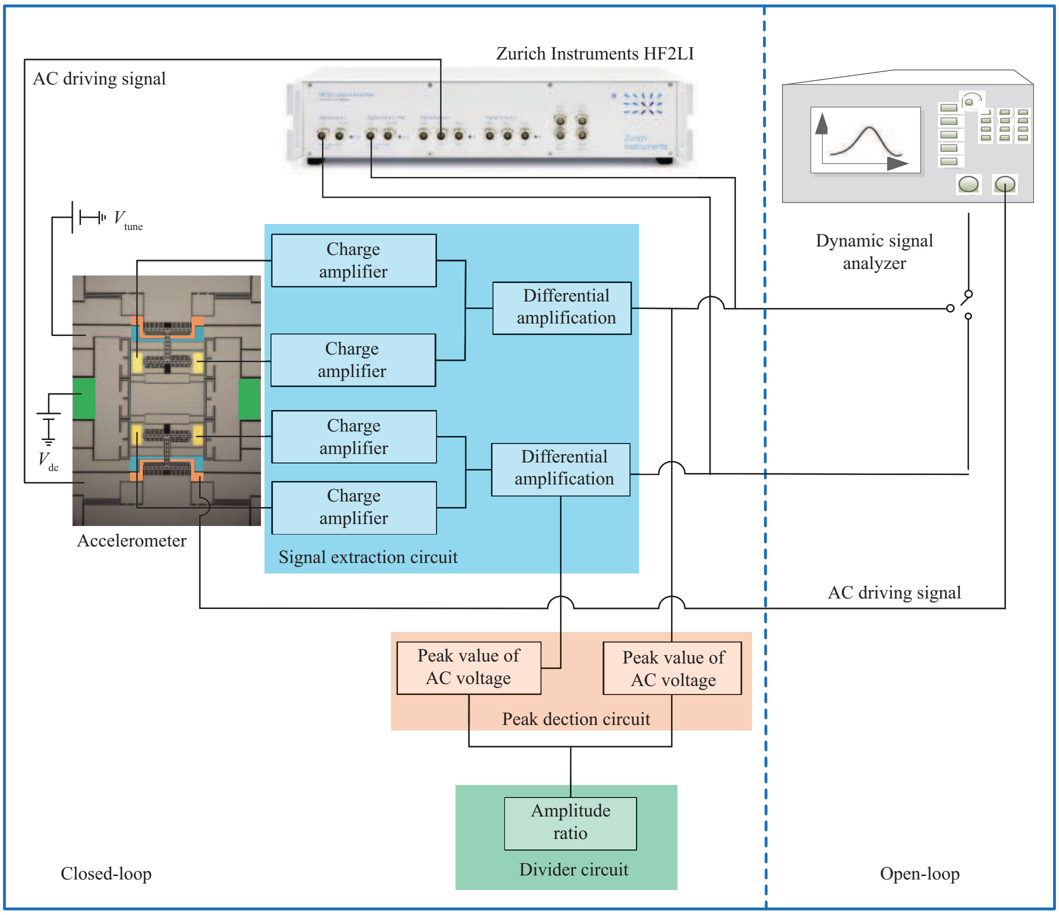

Figure 8 (Color online) Schematic of the open- and closed-loop measurement circuits.

voltage of 5 V was applied to all resonators, and the two proof masses were connected to the ground. An AC sweep signal of 50 mV from a dynamic signal analyzer (DSA) was applied to the drive port of the resonator. The two output current signals from each resonator were first converted to a voltage signal through a charge amplifier (CA) and then sent to the instrumentation amplifier (INA) to eliminate the feedthrough signal. Finally, the output signal of each resonator can be observed on the DSA.

The measurement of the accelerometer in the time domain was realized using a closed-loop self-oscillation circuit implemented based on a previous study [11]. Different from the previous study, the lock-in amplifier and divider circuit were used to obtain one output voltage signal of the amplitude ratio in this measurement scheme. The schematic of the closed-loop measurement circuit comprises a lock-in amplifier (Zurich Instruments HF2LI) and signal extraction, peak detection, and divider circuits (Figure 8). The signal extraction circuit comprises four CAs, which are used to amplify and convert the weak current signals from each resonator into a voltage signal. The INA is used to differentially amplify the signals of the two output electrodes of each resonator to eliminate the feedthrough signal. The lock-in amplifier is used to compensate for the phase difference because the integration operation introduces a phase difference of 90° through CAs. The active peak detection circuit is used to obtain the peak values of the AC output signals of the two resonators. The divider circuit, comprising an analog multiplier and operational amplifier, is used to divide the output signals of the two resonators to make the accelerometer a single-input single-output system. Thus, one voltage signal, which equals the amplitude ratio, is obtained after sending two amplitude signals to the divider circuit. A 5-V DC bias voltage is applied to the DC drive ports, and the output signals are observed on a digital voltmeter. The accelerometer parameters, including sensitivity, bias instability, noise floor, and signal to noise ratio (SNR), are all measured under the closed-loop circumstance. The printed circuit board (PCB) circuit with an accelerometer is fixed on a rotary table, and acceleration can be applied along the sensing direction of the accelerometer by changing the gravitational acceleration component by rotating the table.

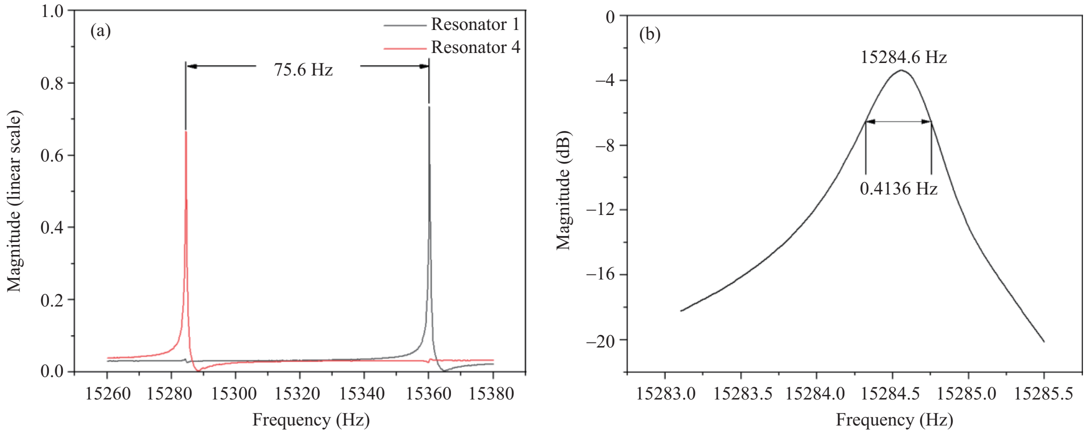

Figure 9 (Color online) (a) Magnitude frequency responses of the accelerometer without acceleration. (b) The 3-dB bandwidth of the accelerometer.

4 Results and discussion

4.1 Frequency responses

Figure 9(a) shows the measured amplitude frequency responses of the 4-DoF accelerometer with no acceleration input. The resonance frequencies of the first two modes are measured as 15284.6 and 15360.2 Hz, respectively. The frequency difference is 75.6 Hz, which is considerably higher than the designed value (0.11 Hz) owing to the fabrication tolerances, causing stiffness or mass mismatch of the two outer resonators.

The mechanical bandwidth of the accelerometer is defined as the frequency range in which the gain at the resonance frequency of the accelerometer decreases by 3 dB. The 3-dB bandwidth of the accelerometer is 0.4136 Hz according to the amplitude frequency response shown in Figure 9(b). Thus, quality factor Q of $15284.6/0.4136 = 36955$ can be obtained.

4.2 Sensitivity

Ideally, the initial working point is at the veering point, which is defined as the point where there is no stiffness perturbation (i.e., no stiffness mismatch between resonators 1 and 4). At this point, the frequency difference between the first two modes is minimum and the amplitude ratio between resonators 1 and 4 is one. However, the stiffness mismatch between resonators 1 and 4, which is caused by the fabrication tolerances, shifts the initial working point away from the veering point; then, the frequency difference between the first two modes becomes larger, and the amplitude ratio is considerably larger than one. Thus, the amplitude of one resonator becomes considerably larger and the other amplitude becomes considerably smaller. It is obvious from Figure 9(a) that only one resonant peak can be detected for each resonator because of the initial working-point shift. Hence, the accelerometer with the output metric of the amplitude ratio cannot be working at the current initial working point. Therefore, the effective stiffness of resonator 1 or 4 should be changed to shift the initial working point to ensure that the amplitude in the first two modes can be measured. Then, the initial working point of 2.12, close to the veering point, is obtained by applying a tuning voltage of −4.7 V to resonator 4. The response to acceleration is measured from 0 to 0.19 g by rotating the rotary table from 0° to 11°.

Figure 10(a) shows the measured amplitude ratios of the accelerometer as a function of the acceleration and the nonlinearity error. The higher acceleration induces a larger amplitude ratio, implying that the amplitude of one resonator becomes extremely small to be detected. The maximum acceleration is 0.19 g in this measurement. When acceleration is larger than 0.19 g, the measurement circuit noise will cover signals of the smaller amplitude variation. Thus, to further extend the sensing range, the ability to measure small amplitudes must be improved. First, it is necessary to reduce the noise of the electronic circuit, which is dominant in the noise of the accelerometer, and some methods are available, such as reducing the power consumption of the circuit, optimizing the selection of electronic components, and using the application specific integrated circuit (ASIC) circuit instead of the PCB circuit. Furthermore, the amplitude of the resonator must be increased by increasing the quality factor of the device and further

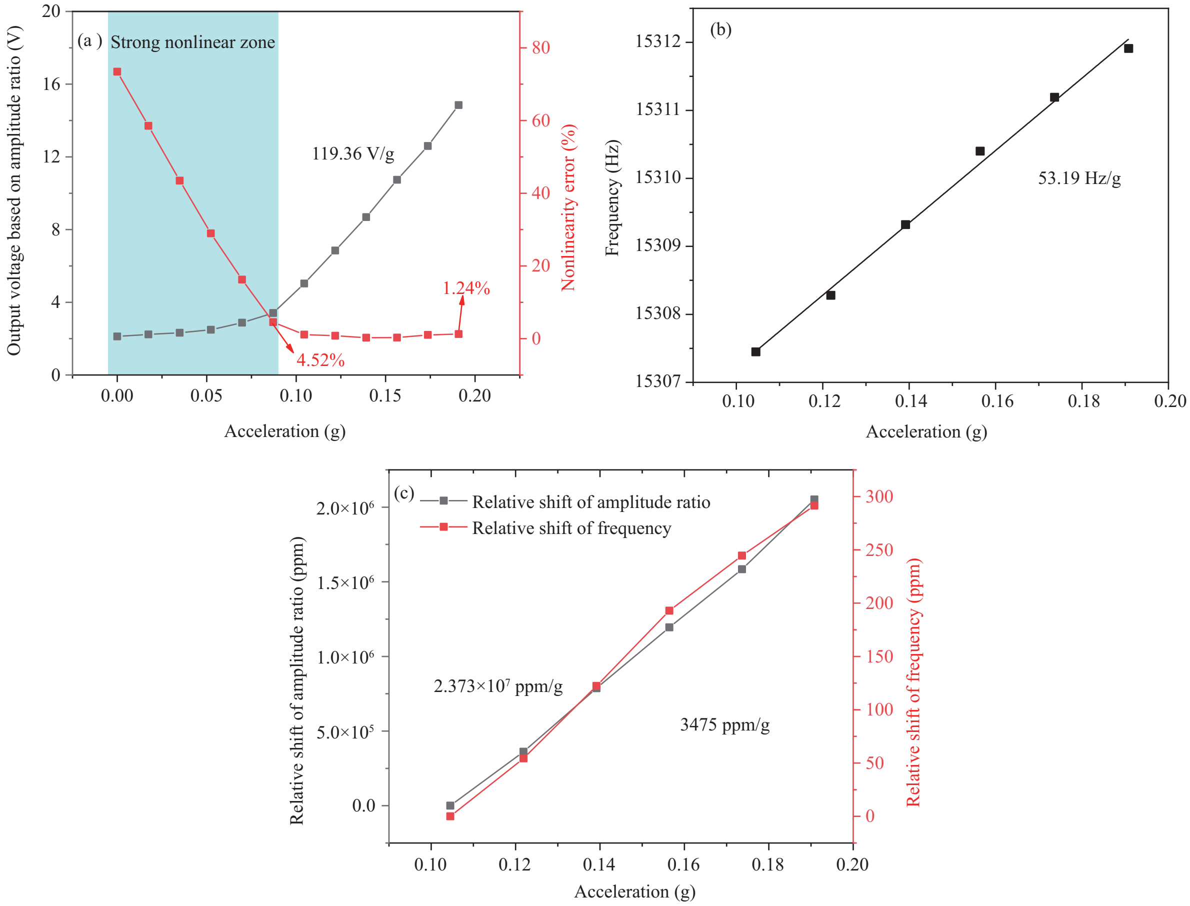

Figure 10 (Color online) (a) Measured output voltage based on the amplitude ratios of the accelerometer as a function of acceleration and the nonlinearity error in open and closed loops. (b) Resonance frequency as a function of acceleration. (c) Relative shift of frequency and amplitude ratio as a function of acceleration.

reducing the impact of the feedthrough signal on the output signal. Moreover, instead of capacitance sensing, optical detection can be considered as an alternative amplitude measurement method to extend the sensing range of the accelerometer. In addition, the measurement environment with constant temperature and vibration-free environment is also needed to reduce the influence of external environment on the accelerometer. Further, the amplitude ratio varies slowly with acceleration, and the minimum nonlinearity error is 4.52% in the blue zone (0–0.104 g). This range is the inherent strong nonlinear zone for mode-localized sensors [25, 26]. The sensitivity and nonlinearity error of the accelerometer are significantly enhanced when the working range is outside the strong nonlinear zone. In the linear zone, the sensitivity and largest nonlinearity error are 119.36 $\mathrm{V{\cdot}g^{-1}}$ and 1.24%, respectively. The sensitivity of the 4-DoF mode-localized accelerometer is enhanced by 2612% and 9042% compared with that of the 3-DoF [12] and 2-DoF [11] mode-localized accelerometers, respectively.

The resonance frequency as a function of acceleration is also measured, and the measured sensitivity is 53.19 $\mathrm{Hz{\cdot}g^{-1}}$ (Figure 10(b)). To compare the sensitivity of the resonance frequency and amplitude ratio in the same scale, the relative sensitivity is calculated as shown in Figure 10(c). The relative sensitivity based on the amplitude ratio (23730000 $\mathrm{ppm{\cdot}g^{-1}}$) is 6828 times higher than that based on the resonance frequency (3475 $\mathrm{ppm{\cdot}g^{-1}}$).

4.3 Bias instability

The bias stability is measured at room temperature without vibration isolation and temperature control. In the measurement, the proof mass is stationary and at the side of WCRs. The output voltages of the accelerometer are recorded for 9100 points with a sampling rate of 10 $\mathrm{points{\cdot}s^{-1}}$ (Figure 11(a)). Then, the accelerometer bias instability of 3.43 μg at an integration time of 6.4 s is obtained by calculating the Allan variance (Figure 11(b)). The bias instability is not as good as the noise floor because of the following

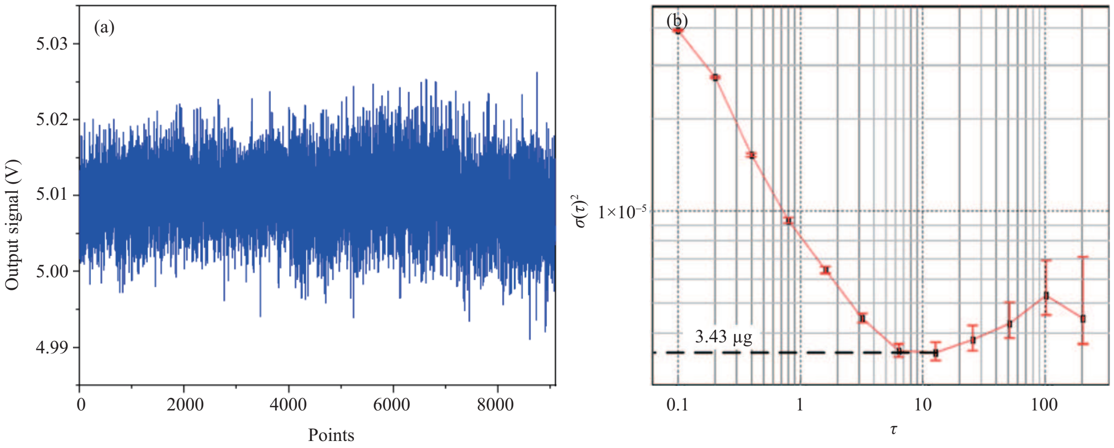

Figure 11 (Color online) (a) Output voltage of the accelerometer. (b) Allan variance of the accelerometer.

reasons: the accelerometer is untested under a constant temperature and vibration-free environment; furthermore, the noise of the measurement circuit in low frequency is large.

4.4 Noise floor

The noise limit of the accelerometer cannot be lower than that of the proof mass, because the acceleration directly acts on the proof mass. First, the quality factor of the proof mass is estimated to obtain the thermal-mechanical noise of the proof mass. The total quality factor Q_{total} of the proof mass and WCRs can be estimated as

$$\frac{1}{Q_{\text{total}}} = \frac{1}{Q_{\text{TED}}} + \frac{1}{Q_{\text{air}}} + \frac{1}{Q_{\text{anchor}}}, \tag{11}$$

where Q_{TED}, Q_{anchor}, and Q_{air} are the quality factor of the thermoelastic, anchor, and air damping, respectively. Q_{TED} and Q_{anchor} of WCRs are simulated as 3.32×10^5 and 2.31×10^7, respectively, using the COMSOL software. Then, Q_{air} of WCRs can be calculated as 4.17×10^4 when the measured Q_{total} is 36955 (Figure 9(b)). Q_{air} of proof mass is assumed to be the same as that of WCRs because the proof mass and WCRs are packaged in the same vacuum environment. Further, Q_{anchor} and Q_{TED} of proof mass are simulated as 1.22×10^8 and 1.76×10^6, respectively. Thus, Q_{total} of proof mass is estimated to be 40738 according to (11). Then, the thermo-mechanical noise of the proof mass can be calculated by [27].

$$a_n = \sqrt{\frac{4K_bT\omega_0}{mQ}}, \tag{12}$$

where K_b is the Boltzmann constant, T is the temperature, and ω_0, m, and Q are the angular frequency, mass, and quality factor of the proof mass, respectively. Based on the parameters in Table 1, the thermal-mechanical noise of proof mass is 13.44 ng·Hz$^{-1/2}$.

The test conditions and environment for the noise floor are the same as those for the bias stability. To obtain the actual noise floor, the FFT results of the output signals in Figure 11 are shown in Figure 12. The system bandwidth is related to the device and measurement circuit and reflects the ability to detect the changing acceleration signals. In this study, the system bandwidth is assumed to be 3 Hz. Thus, the average noise value from 0.01–3 Hz is 0.64 μg·Hz$^{-1/2}$, which is more than one order of magnitude larger than the thermal-mechanical noise value of 13.44 ng·Hz$^{-1/2}$ because of large electronic noise. The noise floor of the 4-DoF mode-localized accelerometer is enhanced by nearly 3 and 2 orders of magnitude compared with the 2-DoF (181 μg·Hz$^{-1/2}$) [11] and 3-DoF (32.4 μg·Hz$^{-1/2}$) [12] mode-localized accelerometer, respectively, using the same FFT method, which shows the effect of DoF on noise improvement of the mode-localized accelerometer.

5 Conclusion

In this paper, we reported a 4-DoF WCRs accelerometer based on a mode localization sensing scheme that can significantly enhance sensor sensitivity significantly. The single-input single-output mode-localized

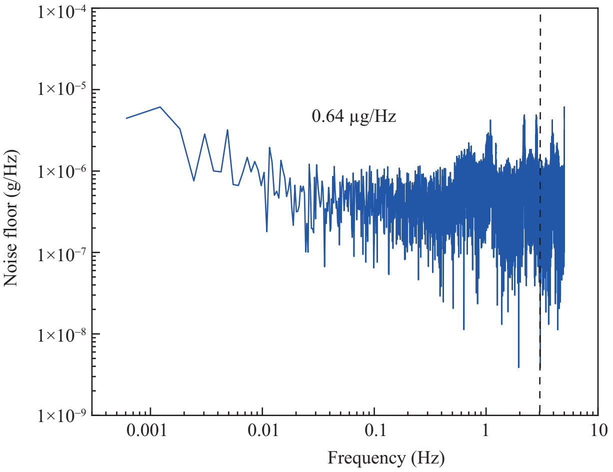

Figure 12 (Color online) Noise spectral density of output signal of the accelerometer.

sensor was realized by using the divider circuit. The closed-loop experimental results showed that sensitivity was significantly improved compared with the 2-DoF and 3-DoF accelerometers, and the noise floor was further improved enhanced, proving that the mode-localized accelerometer with large DoF WCRs is effective to improve the noise floor. The proposed mode-localized accelerometer with a low noise floor is suitable for measuring the signals with the small amplitude and low frequency owing to the limitation of the measurement range (∼0.1 g) and bandwidth (∼3 Hz). Generally, the accelerometer in this paper used herein is suitable for measuring the earthquake and gravitational field changes of the earth for engineering geological survey. Further work will be focused on improving bias instability by optimizing the measurement circuit and measurement conditions.

Acknowledgements This work was supported by the National Key Research and Development Program of China (Grant No. 2018YFB2002600), Shaanxi Key Research and Development Program (Grant No. 2019ZDLGY02-06), Fundamental Research Funds for the Central Universities (Grant No. 3102019JC002), and National Natural Science Foundation of China (Grant No. 51805441).

References

1 Middlemiss R P, Samarelli A, Paul D J, et al. Measurement of the earth tides with a MEMS gravimeter. Nature, 2016, 531: 614–617

2 Zou X D, Thiruvenkatanathan P, Seshia A A. A seismic-grade resonant MEMS accelerometer. J Microelectromech Syst, 2014, 23: 768–770

3 Boom B A, Bertolini A, Hennes E, et al. Nano-G accelerometer using geometric anti-springs. In: Proceedings of the 30th International Conference on Micro Electro Mechanical Systems, Las Vegas, 2017. 33–36

4 Krishnamoorthy U, Olsson Iii R H, Bogart G R, et al. In-plane MEMS-based nano-g accelerometer with sub-wavelength optical resonant sensor. Sens Actuat A-Phys, 2008, 145-146: 283–290

5 Liu C-H, Kenny T W. A high-precision, wide-bandwidth micromachined tunneling accelerometer. J Microelectromech Syst, 2001, 10: 425–433

6 Spletzer M, Raman A, Wu A Q, et al. Ultrasensitive mass sensing using mode localization in coupled microcantilevers. Appl Phys Lett, 2006, 88: 254102

7 Thiruvenkatanathan P, Yan J, Woodhouse J, et al. Ultrasensitive mode-localized mass sensor with electrically tunable parametric sensitivity. Appl Phys Lett, 2010, 96: 081913

8 Zhao C, Wood G S, Xie J, et al. A force sensor based on three weakly coupled resonators with ultrahigh sensitivity. Sens Actuat A-Phys, 2015, 232: 151–162

9 Manav M, Reynen G, Sharma M, et al. Ultrasensitive resonant MEMS transducers with tuneable coupling. J Micromech Microeng, 2014, 24: 055005

10 Zhang H, Li B, Yuan W, et al. An acceleration sensing method based on the mode localization of weakly coupled resonators. J Microelectromech Syst, 2016, 25: 286–296

11 Yang J, Zhong J, Chang H. A closed-loop mode-localized accelerometer. J Microelectromech Syst, 2018, 27: 210–217

12 Kang H, Yang J, Chang H. A closed-loop accelerometer based on three degree-of-freedom weakly coupled resonator with self-elimination of feedthrough signal. IEEE Sens J, 2018, 18: 3960–3967

13 Pandit M, Zhao C, Sobreviela G, et al. A mode-localized MEMS accelerometer with 7 μg bias stability. In: Proceedings of the 31st International Conference on Micro Electro Mechanical Systems, Belfast, 2018. 968–971

14 Pandit M, Zhao C, Sobreviela G, et al. A high resolution differential mode-localized MEMS accelerometer. J Microelectromech Syst, 2019, 28: 782–789

15 Zhang H, Huang J, Yuan W, et al. A high-sensitivity micromechanical electrometer based on mode localization of two degree-of-freedom weakly coupled resonators. J Microelectromech Syst, 2016, 25: 937–946

16 Thiruvenkatanathan P, Yan J, Seshia A A. Ultrasensitive mode-localized micromechanical electrometer. In: Proceedings of 2010 IEEE International Frequency Control Symposium, Newport Beach, 2010. 91–96

17 Zhang H, Chang H, Yuan W. Characterization of forced localization of disordered weakly coupled micromechanical resonators. Microsyst Nanoeng, 2017, 3: 17023

18 Zhong J, Yang J, Chang H. The temperature drift suppression of mode-localized resonant sensors. In: Proceedings of the 31st International Conference on Micro Electro Mechanical Systems, Belfast, 2018. 467–470

19 Thiruvenkatanathan P, Yan J, Seshia A A. Common mode rejection in electrically coupled MEMS resonators utilizing mode localization for sensor applications. In: Proceedings of 2009 IEEE International Frequency Control Symposium Joint with the 22nd European Frequency and Time Forum, Besancon, 2009. 358–363

20 Pandit M, Zhao C, Sobreviela G, et al. Practical limits to common mode rejection in mode localized weakly coupled resonators. IEEE Sens J, 2020, 20: 6818–6825

21 Zhang H, Zhong J, Yuan W, et al. Ambient pressure drift rejection of mode-localized resonant sensors. In: Proceedings of the 30th International Conference on Micro Electro Mechanical Systems, Las Vegas, 2017. 1095–1098

22 Kang H, Yang J, Chang H. A mode-localized accelerometer based on four degree-of-freedom weakly coupled resonators. In: Proceedings of the 31st International Conference on Micro Electro Mechanical Systems, Belfast, 2018. 960–963

23 Thomson W. Theory of Vibration With Application. Boca Raton: CRC Press, 2018

24 Hao Y, Yuan W, Xie J, et al. Design and verification of a structure for isolating packaging stress in SOI MEMS devices. IEEE Sens J, 2017, 17: 1246–1254

25 Zhang H, Kang H, Chang H. Suppression on nonlinearity of mode-localized sensors using algebraic summation of amplitude ratios as the output metric. IEEE Sens J, 2018, 18: 7802–7809

26 Zhang H, Yang J, Yuan W, et al. Linear sensing for mode-localized sensors. Sens Actuat A-Phys, 2018, 277: 35–42

27 Gabrielson T B. Mechanical-thermal noise in micromachined acoustic and vibration sensors. IEEE Trans Electron Devices, 1993, 40: 903–909